Supplementary Information for:

Solvation Effects in the Electrochemical Reduction of Hydrogen Cyanide for Ambient Ammonia Production on a Ni Cathode

Kevin Brennan,[a] Graeme W. Watson,[a] Max García-Melchor[a,b,*]

[a] *School of Chemistry, Trinity College Dublin, College Green, Dublin 2, Ireland.*

[b] *CRANN and AMBER Research Centres, College Green, Dublin 2, Ireland.*

Contents

1. Gibbs Energy Corrections

For every intermediate, the Thermochemistry module implemented in the Atomic Simulation Environment (ASE) package was used to calculate Gibbs energy corrections in the harmonic limit.[1] All thermodynamic corrections were calculated at standard conditions, *i.e.* 298.15 K and 1 atm. The reported Helmholtz energies (F) were calculated as: $F = U - TS$.

Table S1. Gibbs energy corrections (in eV) for the HCNRR intermediates in the presence of vacuum, implicit, and explicit solvent. For further details, see the Computational Methods section in the main text. The asterisk (*) in the intermediates denotes a chemisorbed species.

Vacuum					
Intermediate	**ZPE**	**C_{vib}**	**U**	**T*S**	**F**
HCN	0.453	0.091	0.545	0.224	0.321
*CHNH	0.803	0.089	0.892	0.188	0.704
CH_2NH	1.084	0.088	1.172	0.225	0.947
*CH_2NH_2	1.473	0.104	1.577	0.213	1.363
CH_3NH_2	1.741	0.147	1.888	0.362	1.525
CH_3NH_3	2.095	0.140	2.236	0.323	1.912
*CH_3 + NH_3	1.923	0.171	2.095	0.397	1.698
*CH_3 + $NH_{3(g)}$	0.971	0.067	1.038	0.124	0.914
CH_4 + NH_3	2.171	0.191	2.361	0.470	1.891
CH_4 + $NH_{3(g)}$	1.220	0.088	1.308	0.226	1.082
Implicit Solvation					
Intermediate	**ZPE**	**C_{vib}**	**U**	**T*S**	**F**
HCN	0.457	0.116	0.573	0.313	0.256
*CHNH	0.804	0.087	0.891	0.179	0.712
CH_2NH	1.087	0.089	1.177	0.244	0.932
*CH_2NH_2	1.470	0.108	1.578	0.218	1.360
CH_3NH_2	1.738	0.150	1.888	0.439	1.449
CH_3NH_3	2.140	0.120	2.261	0.275	1.986
*CH_3 + NH_3	1.916	0.175	2.091	0.390	1.701
*CH_3 + $NH_{3(g)}$	0.970	0.068	1.038	0.127	0.911
CH_4 + NH_3	2.142	0.084	2.26	0.194	2.032
CH_4 + $NH_{3(g)}$	1.231	0.101	1.332	0.231	1.101

Explicit Solvation					
Intermediate	**ZPE**	**C$_{vib}$**	**U**	**T*S**	**F**
HCN	0.750	0.084	0.834	0.167	0.667
CHNH	0.695	0.99	0.794	0.208	0.587
CH$_2$N	0.715	0.120	0.835	0.275	0.560
CH$_2$NH	1.129	0.111	1.240	0.238	1.002
CH$_2$NH$_2$	1.465	0.110	1.575	0.216	1.359
CH$_3$NH$_2$	1.786	0.124	1.910	0.263	1.647
CH$_3$NH$_3$	2.154	0.126	2.280	0.267	2.013
*CH$_3$ + NH$_3$	1.984	0.155	2.139	0.297	1.842
*CH$_3$ + NH$_{3(g)}$	0.965	0.069	1.034	0.130	0.904
CH$_4$ + NH$_3$	2.235	0.196	2.431	0.436	1.996
CH$_4$ + NH$_{3(g)}$	1.235	0.125	1.360	0.316	1.044

2. Bader Charge Analysis

Table S2. Computed Bader charges (in a.u.) for each HCNRR intermediate modelled with an explicit water bilayer. The values of q_{mol} denote the Bader charges of each intermediate, while q_{water} and q_{slab} represent the sum of charges on atoms comprising the explicit water bilayer and the net charge of the Ni slab with the H coverage, respectively.

Intermediate	q_{mol}	q_{water}	q_{slab}
Water Bilayer	-	–0.002	+0.002
H^+ Water Bilayer	-	+0.726	–0.726
HCN	–0.112	+0.626	–0.514
CHNH	+0.195	+0.035	–0.230
CH_2N	–0.003	–0.070	0.074
CH_2NH	+0.031	–0.040	–0.010
CH_2NH_2	+0.470	–0.142	–0.328
CH_3NH_2	+0.046	–0.090	+0.044
CH_3NH_3	+0.774	–0.125	–0.649
$*CH_3 + NH_3$	+0.004	–0.046	+0.050
$*CH_3$	–0.065	–0.005	+0.069
$CH_4 + NH_3$	+0.023	–0.040	+0.017
CH_4	–0.009	–0.001	+0.010

3. Charge Density Difference Analysis

Charge density differences (ρ_{diff}) were calculated as follows:

$$\rho_{diff} = \rho_{tot} - \rho_{surf} - \rho_{ads} \#(1)$$

Where ρ_{tot} denotes the total charge density of the system, and ρ_{surf} and ρ_{ads} are the charge density of the surface and adsorbate fragments calculated via single-point calculations, respectively.
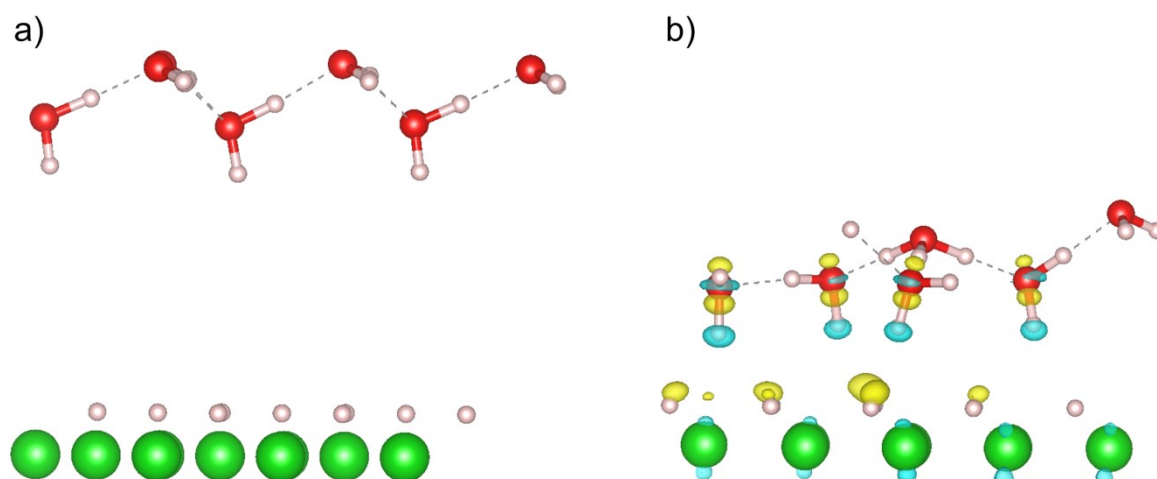

Figure S1. Representation of the charge density difference (isovalue = 0.0035 a.u) calculated for the a) neutral water bilayer, composed of six H_2O molecules, and (b) protonated water bilayer, comprising five H_2O molecules and one H_3O^+ molecule above the cathode surface. Yellow (blue) isosurfaces represent an increase (decrease) in electron charge density. Color code: C (grey), H (white), O (red), Ni (green).

As expected, the neutral water layer in Figure S1a displays no charge. The protonated system shown in Figure S1b, however, displays an accumulation of positive charge in the H-down water molecules and negative charge localized on the surface H atoms. These charge accumulations confirm the separation of the proton and electron to the water layer and the electrode, respectively, effectively mimicking the electrochemical double layer.
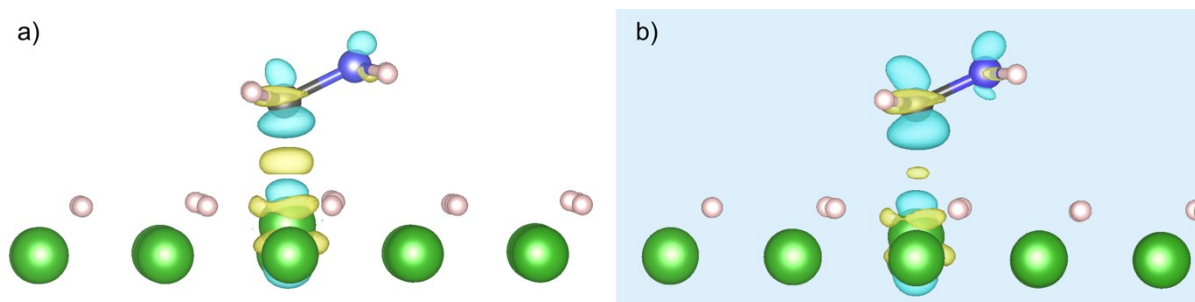
Figure S2. Representation of the charge density difference (isovalue = 0.006 a.u) calculated for the *CH$_2$NH$_2$ intermediate in the presence of a) vacuum, and (b) a dielectric continuum. Yellow (blue) isosurfaces represent an increase (decrease) in electron charge density. Color code is the same as in Figure S1.

The presence of increased electron density between the C atom and the Ni cathode implies the presence of a bonding interaction, although it is interesting to note that the magnitude of the bonding interactions varies across both phases. The weaker interaction between *CH$_2$NH$_2$ and the Ni surface in implicit solvent is to be expected due to the larger distance between the two.

4. Transition State Calculations

Transition states were located via climbing image nudged elastic band (CI-NEB) calculations and confirmed by the presence of only one imaginary vibrational frequency. For each CI-NEB, eight images were optimized between the initial and final states. The image dependent pair potential[2] was used to provide an initial guess for the structures between the initial and final states. We present an example below for the direct formation of CH_2N from HCN.
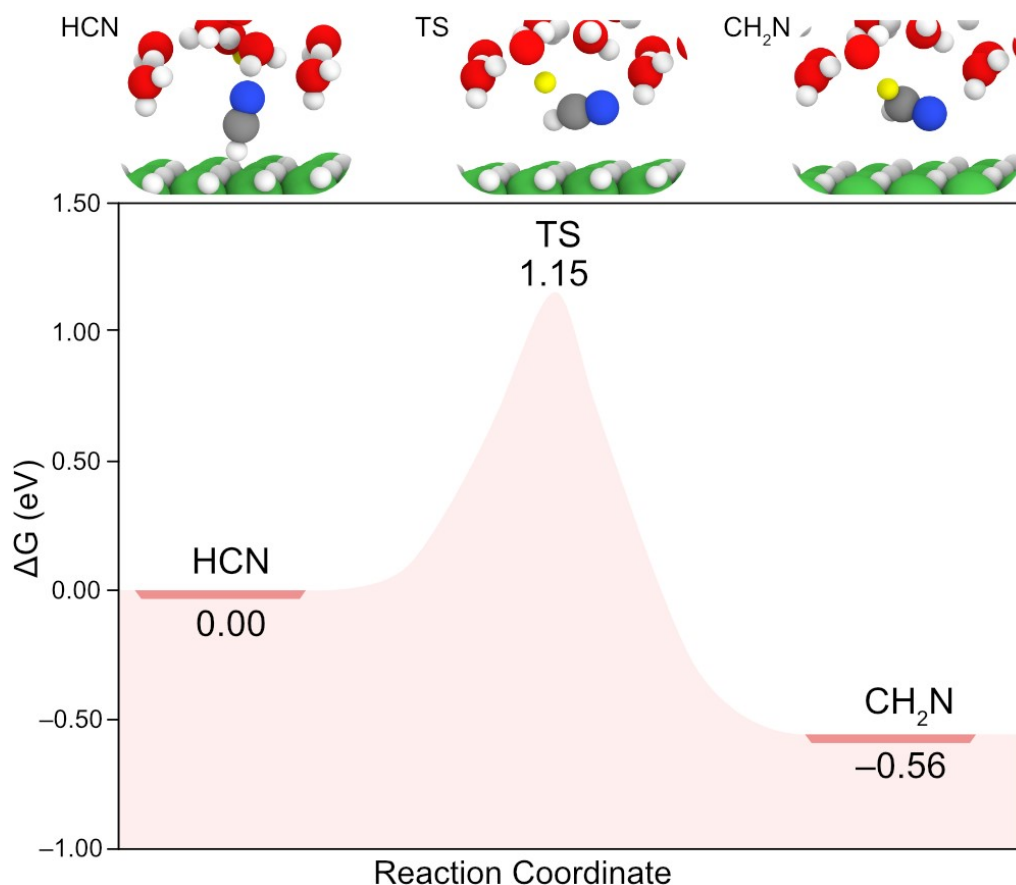

Figure S3. CI-NEB for the direct formation of CH_2N from HCN. Gibbs energies (in eV) are relative to the initial state, that is the adsorbed HCN on the predicted resting state of the Ni(111) slab with all the *fcc* sites covered by H atoms. The atom highlighted in yellow refers to the H involved in the transition state for this hydrogenation step. Color code: C (grey), H (white), N (blue), O (red), Ni (green).

5. Non-Covalent Interactions

Non-covalent interactions (NCIs) were computed using the Critic2 software,[3,4] which calculates the reduced density gradient, $s(\rho)$, from the electron density ρ according to:

$$s(\rho) = \frac{1}{2(3\pi^2)^{\frac{1}{3}}} \frac{|\nabla\rho(r)|}{\rho(r)^{\frac{4}{3}}} \#(2)$$

The reduced density gradient between interacting atoms can change quite drastically due to weak intra- or intermolecular interactions, leading to density critical points between fragments defined by the user. Troughs can be seen in the reduced gradient density due to these bond critical points. Both attractive and repulsive interactions can appear in the same reduced density gradient region. The curvature of the density must be examined to determine the nature of these interactions. This is done by inspecting the eigenvalue contributions to the second derivative electron density matrix, also known as the Hessian matrix, λ_i, so that $\nabla^2\rho(r) = \lambda_1 + \lambda_2 + \lambda_3$. The sign of the second eigenvalue, λ_2, is used to determine whether an interaction is repulsive or attractive.[5]

Increased electron density perpendicular to a bond critical point denotes an attractive interaction and is characterized via $\lambda_2 < 0$. Conversely, repulsive interactions, where density is depleted at these critical points, are observed with $\lambda_2 > 0$. Consequently, we can plot the reduced density gradient against the sign of λ_2 multiplied by the electron density ρ to observe the various non-covalent interactions between user-defined fragments of a system.

NCIs were calculated between three different fragments: i) the resting state of the Ni slab (including the H coverage), ii) the HCNRR intermediate, and iii) the explicit solvent molecules.
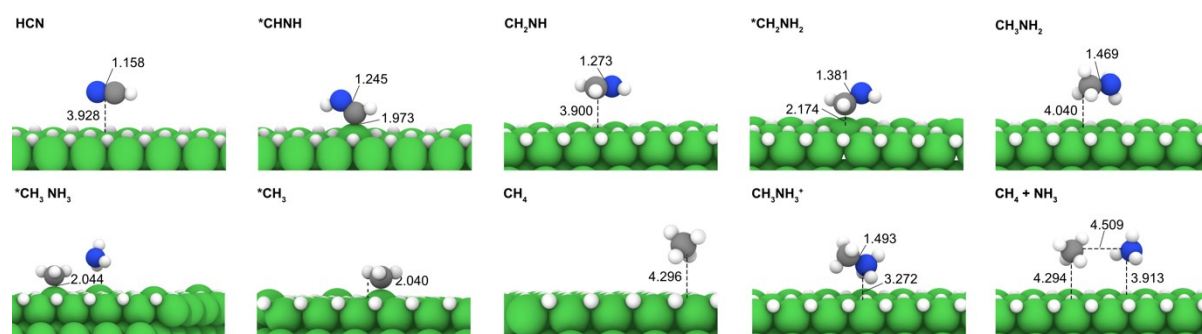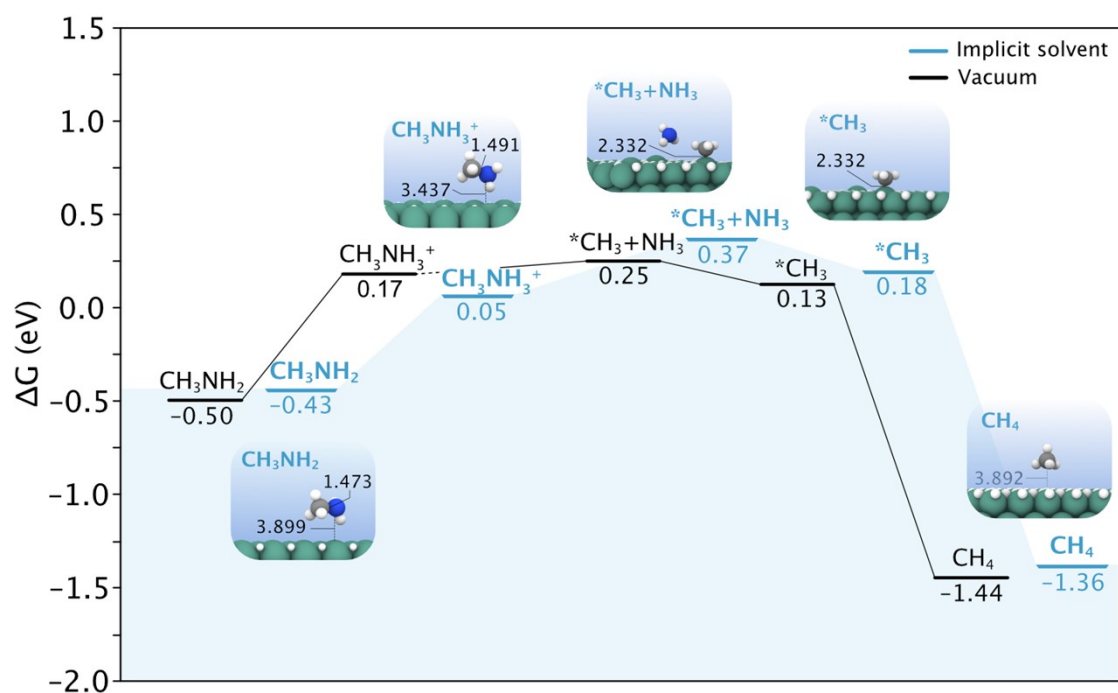
6. Vacuum Phase HCNRR Structures

Figure S4. Intermediates involved in the HCNRR under vacuum conditions. Relevant bond lengths are given in Å. The color code used is the same as in Figure S3.

7. Alternative Pathways

Figure S5. Alternative pathway for the formation of CH_4 and NH_3 in vacuum (black) and implicit solvent (blue).
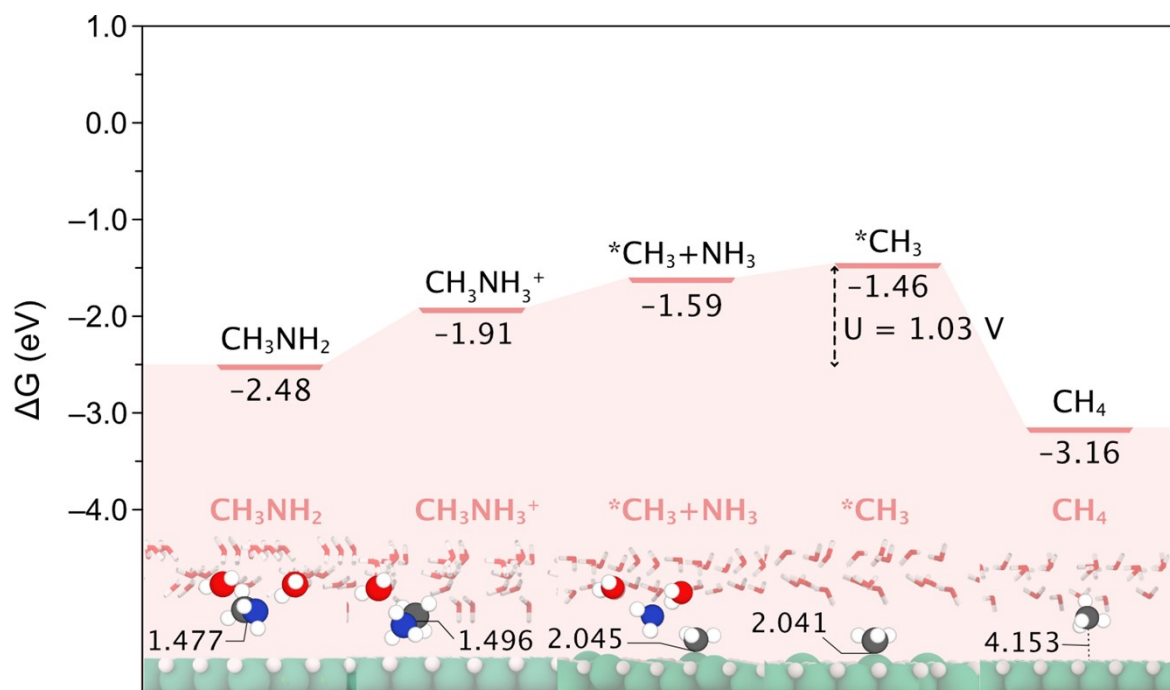
Figure S6. Alternative pathway for the formation of CH_4 and NH_3 in the presence of an explicit water bilayer.

8. Comparison with Gas Phase Energies

Table S3. Overall reaction energies calculated for the 4- and 6-electron HCNRR leading to methylamine, and methane and ammonia, respectively. These energies are calculated as the difference in the gas phase energies of products and reactants, with the energy of a proton and electron pair being equated to half of the energy of H_2, according to the computational hydrogen electrode model, as described in the Computational Methods in the main text.

	Original (eV)	Corrected (eV)	Exp. (eV)
$HCN + 4H^+ + 4e^- \rightarrow CH_3NH_2$	−0.62	−1.07	−0.95
$HCN + 6H^+ + 6e^- \rightarrow CH_4 + NH_3$	−1.55	−2.06	−1.99

We observe the original reaction energies, calculated without gas phase corrections, deviate from the experimental values, derived from the standard redox potentials. The formation of CH_3NH_2, when the gas phase species are uncorrected, suffers from a relative error of 34.9%. This error is reduced to only 11.8% when gas phase errors are applied following the procedure developed by Calle-Vallejo *et al.*[6] Similarly, the formation energy of CH_4 and NH_3 is significantly improved with gas phase corrections, with the calculated relative error improving from 21.9% to 3.5%.

However, despite these excellent agreements with experiments, we have chosen to not include the corrections for gas phase errors. The rationale behind this decision is the lack of analogous corrections for species in the liquid phase. We also do not believe that corrections calculated in the gas phase can be applied to species calculated in an implicit solvent. We also note that, as only the energy of HCN would be corrected, the result would be an overall shift equal to the correction. As such, the overall conclusions, *i.e.,* the potential limiting steps, would not change.

9. Examination of Ionic Effects in Implicit Solvent

As the calculation of the HCNRR intermediates in the presence of the dielectric continuum employ the linearized Poisson-Boltzmann equation, they also account for ionic effects. However, the intermediates calculated with explicit solvent molecules neglect these ionic effects. For the purposes of comparison, we have investigated whether ionic effects have a significant impact on the energies of intermediates in implicit solvent, with the results summarized in Table S4.

Table S4. Energies of HCNRR intermediates in implicit solvent with only solvent effects, labelled as E_{solv}, and with both solvent and ion effects, $E_{(ion + solv)}$. We also include the difference between these energies for the same intermediate in the rightmost column.

Intermediate	E_{solv} / eV	$E_{(ion + solv)}$ / eV	ΔE / eV
HCN	−172.5812	−172.5822	0.0003
*CHNH	−175.8335	−175.8339	0.0004
CH$_2$NH	−180.6782	−180.6782	0.0001
*CH$_2$NH$_2$	−184.5642	−184.5642	0.0000
CH$_3$NH$_2$	−189.3626	−189.3628	0.0002
CH$_3$NH$_3^+$	−193.1619	−193.1593	−0.0026
CH$_4$ + NH$_3$	−198.0602	−198.0606	0.0004

It can be seen in the above table that the difference in energies with and without ionic effects are negligible, being only present in the third decimal at most. As such, the differences between the explicit and implicit solvation models cannot be attributed to the absence of ionic effects in the explicit solvent.

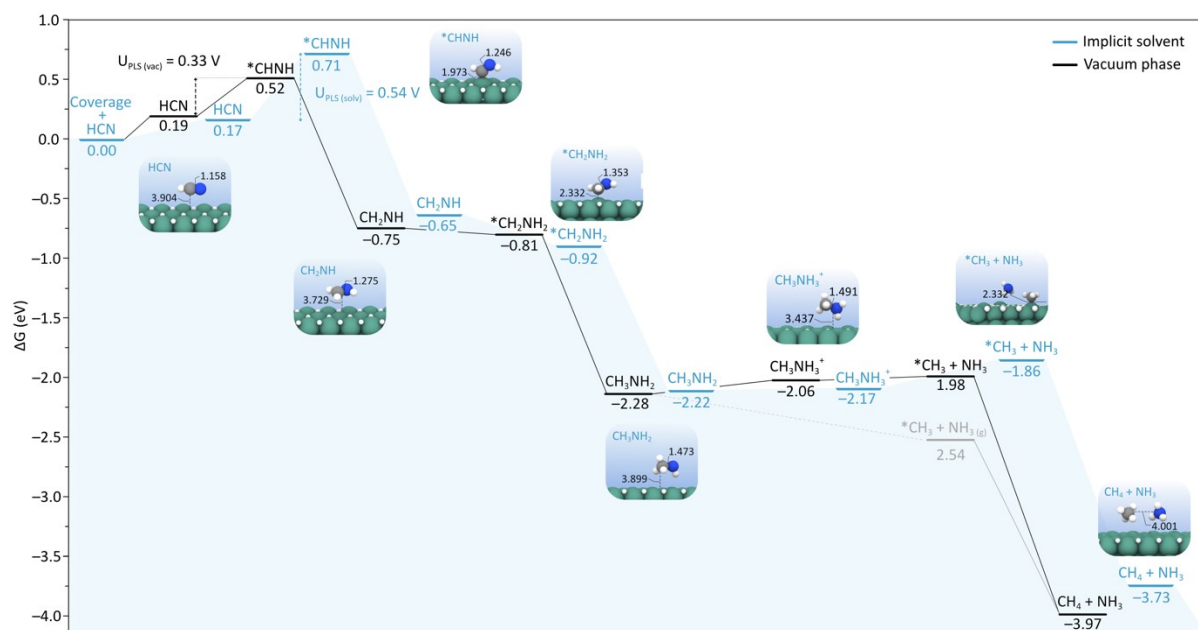## 10. HCNRR Pathways under Experimental Conditions

Figure S7. Gibbs energy profile for the HCNRR modelled in vacuum (black) and implicit solvent (blue) under the experimental conditions of –0.8 V_{SHE} and pH 6.
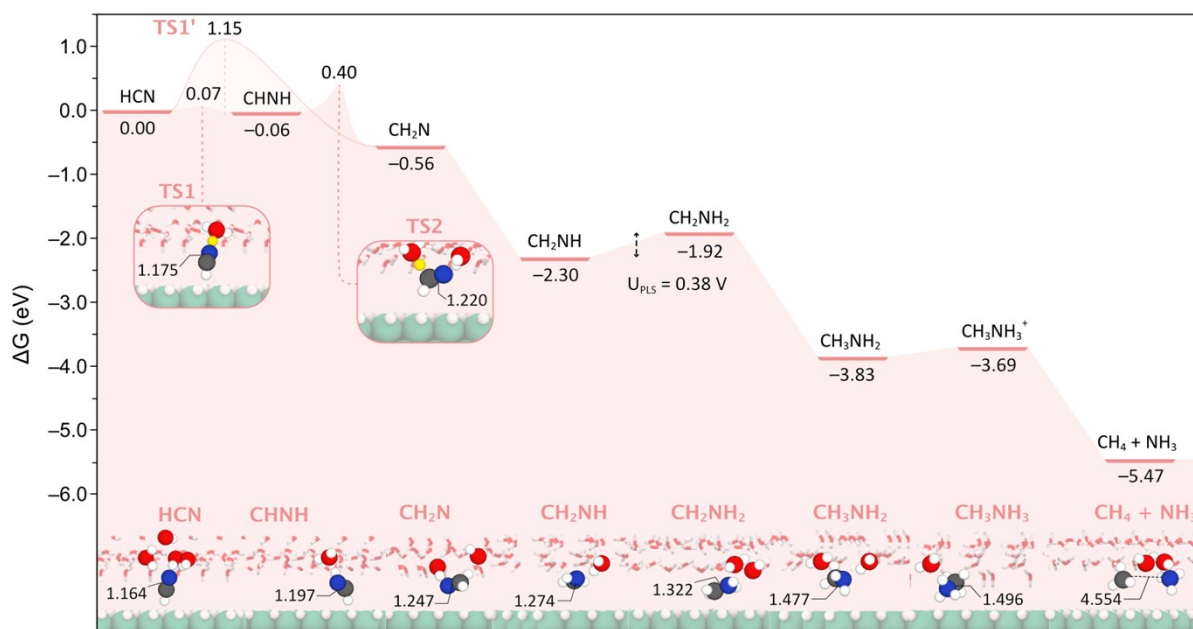

Figure S8. Gibbs energy profile for the HCNRR modelled with explicit solvent under the experimental conditions of –0.8 V_{SHE} and pH 6.

11. Fermi Levels

To assess the influence of the different solvation models on the Fermi levels, we have plotted in Figure S9 the Fermi levels of the HCNRR intermediates involved in all three pathways.

Upon initial inspection, a substantial difference in the Fermi levels of the intermediates calculated in implicit solvent compared to the vacuum phase is apparent. It is however essential to note that the reference potential with implicit solvent is aligned with that of the bulk electrolyte,[7] causing a shift in the Fermi levels due to the zero average electrostatic potential in the simulation cell.

To thoroughly assess the impact on our findings, we have examined the variation of the Fermi levels across intermediates within the same phase. For instance, the change in Fermi level from CH_3NH_2 to $CH_3NH_3^+$ is observed to be +1.46, +1.32, and +1.05 eV in vacuum, implicit solvent, and explicit solvent, respectively. While there is a non-negligible difference between these values, we believe that it may not fully account for the observed change in the relative Gibbs energies, which we attribute to site-specific effects such as H bonding with the water bilayer.
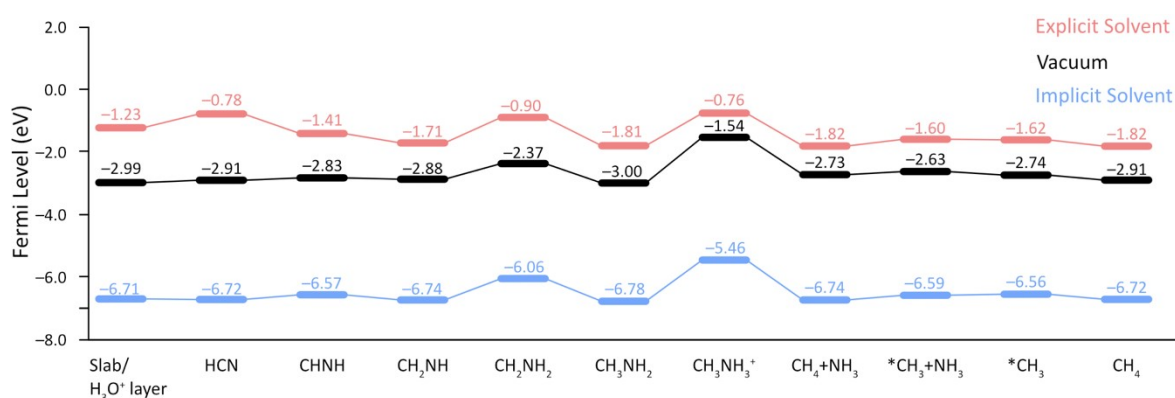

Figure S9. Plot of the Fermi levels calculated for the HCNRR intermediates calculated in vacuum (black), implicit solvent (blue), and explicit solvent (red) phases.

12. Cartesian Coordinates

All cartesian coordinates, including visualized optimized geometries, energies, and magnetizations for each modelled intermediate and TS can be found in the following ioChem-BD dataset:

https://iochem-bd.bsc.es/browse/review-collection/100/304455/e9c963f4409ec334bad3bb0b

13. References

1 A. Hjorth Larsen, J. Jørgen Mortensen, J. Blomqvist, I. E. Castelli, R. Christensen, M. Dułak, J. Friis, M. N. Groves, B. Hammer, C. Hargus, E. D. Hermes, P. C. Jennings, P. Bjerre Jensen, J. Kermode, J. R. Kitchin, E. Leonhard Kolsbjerg, J. Kubal, K. Kaasbjerg, S. Lysgaard, J. Bergmann Maronsson, T. Maxson, T. Olsen, L. Pastewka, A. Peterson, C. Rostgaard, J. Schiøtz, O. Schütt, M. Strange, K. S. Thygesen, T. Vegge, L. Vilhelmsen, M. Walter, Z. Zeng and K. W. Jacobsen, *J. Phys. Condens. Matter*, 2017, **29**, 273002.

2 S. Smidstrup, A. Pedersen, K. Stokbro and H. Jónsson, *J. Chem. Phys.*, 2014, **140**, 214106.

3 A. Otero-de-la-Roza, M. A. Blanco, A. M. Pendás and V. Luaña, *Comput. Phys. Commun.*, 2009, **180**, 157–166.

4 A. Otero-de-la-Roza, E. R. Johnson and V. Luaña, *Comput. Phys. Commun.*, 2014, **185**, 1007–1018.

5 J. Contreras-García, E. R. Johnson, S. Keinan, R. Chaudret, J.-P. Piquemal, D. N. Beratan and W. Yang, *J. Chem. Theory Comput.*, 2011, **7**, 625–632.

6 R. Urrego-Ortiz, S. Builes and F. Calle-Vallejo, *ChemCatChem*, 2021, **13**, 2508–2516.

7 K. Mathew, V. S. C. Kolluru, S. Mula, S. N. Steinmann and R. G. Hennig, *J. Chem. Phys.*, 2019, **151**, 234101.